Oxidation of Metals (2021) 96:307–321
https://doi.org/10.1007/s11085-021-10048-5

ORIGINAL PAPER

Oxidation Behavior of $Al_x(CoCrFeNi)_{100-x}$ High-Entropy Alloys Under Thermal-Cycling Conditions

J. Dąbrowa[1] · G. Cieślak[2] · M. Stygar[1] · M. Zajusz[1] · M. Jawańska[1] · A. Gil[1] · J. Jedliński[1] · K. Mroczka[3] · K. Matsuda[4] · T. Kulik[2] · M. Danielewski[1]

Received: 30 May 2021 / Revised: 30 May 2021 / Accepted: 1 June 2021 /
Published online: 25 July 2021

Abstract

The oxidation behavior of five different high-entropy alloys from the Al–Co–Cr–Fe–Ni metallic system, namely $Al_x(CoCrFeNi)_{100-x}$ ($x = 0$; 3; 6; 9; 12), was studied under thermal-cycling conditions, at 1273 K in air atmosphere. The choice of selected compositions allowed for covering the chromia-to-alumina former transition, as well as the transition from the FCC single-phase solid solution structure to multiphase alloys with Al-enriched B2-structured constituent. The measurements were taken for 500 cycles (1 cycle - 1 h of heating, 20 min of cooling). The results indicate a profound influence of the thermal-cycling conditions on the oxidation products, with extremely complex scale structures and extensive internal oxidation and nitridation zones, as well as severe spallation of the oxide scale in most cases, showing the limited usefulness of these alloys for high-temperature applications at the current stage of their development.

Keywords High-entropy alloys · Superalloys · Thermal-cycling · Chromia formers · Alumina formers

✉ J. Dąbrowa
dabrowa@agh.edu.pl

[1] Faculty of Materials Science and Ceramics, AGH University of Science and Technology, al. Mickiewicza 30, 30-059 Kraków, Poland

[2] Faculty of Materials Science and Engineering, Warsaw University of Technology, ul. Wołoska 141, 02-507 Warszawa, Poland

[3] Institute of Technology, Pedagogical University of Cracow, ul. Podchorążych 2, 30-084 Kraków, Poland

[4] Department of Materials Science and Engineering, University of Toyama, Toyama, Japan

Introduction

High-entropy alloys (HEAs) are currently among the most extensively researched metallic materials. The first concept of HEAs was presented by Yeh and Huang in 1995 [1]; however, it was not until 2004 when HEAs were recognized by the wider public [2, 3]. The entire concept of the high-entropy approach was based on two main motivations: an investigation of the vast, yet unexplored central regions of multicomponent phase diagrams [3] and investigation of the possibility of stabilizing the single-phase solid solution structures over intermetallic phases by controlling the configurational entropy in complex alloys [4]. Initially, the term 'high-entropy alloy' applied only to equimolar or near-equimolar compositions of five or more elements [2] but later was expanded to quaternary systems and high-entropy systems with minor additives, enabling further modification of their properties [5]. After over 15 years of development, the range of known HEA compositions has greatly expanded, with many of them exhibiting excellent thermomechanical properties and high melting temperatures, good room-temperature ductility, good phase stability, high fracture toughness, as well as creep and fatigue resistance [6–8]. Among them, the multiphase, precipitation-strengthened, *3d* transition metal-based HEAs (TM-HEAs) are probably attracting the most interest as they appear to be a natural extension of the superalloys concept to the high-entropy regions of phase diagrams. As a result, they are often regarded as a potential replacement for the state-of-the-art, nickel-based superalloys in the structural, high-temperature applications [7, 9, 10]. However, from such point of view, apart from the extraordinary mechanical properties at high temperatures already possessed by selected HEAs [11–13], sufficient corrosion resistance understood as both heat and creep resistance is equally as important and, in fact, remains the main limiting factor for the current TM-HEAs. Therefore, there is an urgent need for its further investigation, especially considering the current lack of the experimental, non-isothermal data and well-developed theories enabling a sufficient description of the gaseous corrosion of HEAs. One of the challenges in terms of a systematic approach to the subject of high-temperature oxidation of HEAs is a vast number of possible compositions. As of today, two parent systems of the highest popularity can be distinguished for the TM-HEA compositions, namely Co–Cr–Fe–Ni (face-centered cubic - FCC-structured, chromia-forming alloys) and Al–Cr–Co–(Cu–)Fe–Ni (FCC/body-centered cubic - BCC/B2-structured, chromia and alumina forming alloys) [9]. In the latter case, it can be observed that with the proceeding development of HEAs' metallurgy Cu has been systematically removed from the system, as the Cu-containing compositions have been reported to exhibit a strong tendency toward the formation of Cu-rich phases [14, 15] and very poor scales adhesion [16]. The resulting Al–Cr–Co–Fe–Ni alloys are probably the most studied materials in the HEA family [17], thanks to the promising thermomechanical properties and possibility of tailoring their phase compositions in a relatively straightforward manner. Microstructures and properties of $Al_xCoCrFeNi$ alloys (with x varying from 0 to 2) were extensively studied by Kao et al. [18, 19], revealing that Al content is a

decisive factor in terms of their structure, mainly due to the fact of being by far the biggest atom in the system, as well as the strongest BCC former, which can be explained on the basis of its relatively low value of valence electron concentration (VEC) [9]. Furthermore, big atomic radius of Al plays a crucial role in establishing the high mechanical properties of the BCC phase, as it increases the distortion of the lattice and slip resistance [14].

The isothermal oxidation behavior has been examined relatively thoroughly in Al–Co–Cr–Fe–Ni system. In particular, the influence of Al content on oxidation behavior and oxidation kinetics at various temperatures has been elaborated in multiple studies [20–24]. It is worth noting that despite a complete lack of studies dedicated to the oxidation behavior of this group of HEAs under thermal-cycling conditions, their behavior in isothermal conditions already shows a profound tendency toward scale spallation during cooling [6, 21], a quality disqualifying for practically all real-life applications. First significant, and currently by far the most extensive and influential works in the field of the high-temperature corrosion of HEAs, have been authored by the group of Butler et al. In their very first study, high-temperature oxidation behavior of the alloys from Al–Co–Cr–Ni–(Fe or Si) systems was investigated to '*provide some insights into oxidation behavior of HEAs*' [20]. The observed oxide scale formation was interpreted in the light of the Giggins–Pettit theory originally developed to describe the behavior of the Ni–Cr–Al alloys [25]. The Giggins–Pettit theory divides the Ni-based superalloys into three groups depending on the scale composition and structure:

- **group I** corresponds to alloys with Al and Cr content too low to form continuous, protective scales of either Cr_2O_3 or Al_2O_3. Hence, the scale consists of NiO and $NiCr_2O_4$ or $Ni_2Al_2O_4$ spinel phases with internal oxidation zone of Al.
- **group II** consists of the alloys with relatively high content of Cr and low of Al. Therefore, the continuous chromia scale forms via selective oxidation, with the internal oxidation zone of Al.
- **group III** corresponds to the alloys with Al content high enough to promote its selective oxidation and the formation of a continuous Al_2O_3 scale.

In the work of Butler et al. [21], the Giggins–Pettit theory allowed predicting the scale's composition and structure, based solely on the Al and Cr contents in the initial HEAs, with the sum of the rest of the elements being considered as Ni equivalent. As a result, it was proved experimentally that certain HEA systems can be considered analogs of Ni–Cr–Al alloys in terms of the high-temperature corrosion investigations under isothermal conditions [20]. T*x*he results also provided extremely important information that the selective oxidation of Al and Cr actually takes place in HEAs. The subsequent study by the same group focused on the investigation of the dependence of the structure and oxidation behavior of the $Al_x(CoCrFeNi)_{100-x}$ alloys on the Al content [21]. The corrosion study included isothermal oxidation in the air for 50 h at 1050 °C. The oxidized microstructures were again consistent with the expectations of the Giggins–Pettit theory, and the investigated alloys were classified into II and/or III group, according to the abovementioned classification, with the transition between these regimes taking place for

$x = 8$ and 10. The increased Al content promoted the formation of the protective alumina scale with the $Al_{30}(CoCrFeNi)_{70}$ exhibiting the best oxidation resistance. All of the alloys were characterized by the parabolic oxide growth kinetics proceeded by a short initial transient oxidation. Further studies of the same group focused on the influence of thermal pre-treatment on the oxidation behavior of the alloys from the same system [26].

In the case of the Co–Cr–Fe–Ni-based systems in which the formation of protective scales can be based strictly on the chromia formation, the available high-temperature data are much more fragmentary. Probably the most extensive study in this field was conducted by Holcomb et al. [27] who studied the oxidation of the so-called Cantor alloy, *i.e.*, equimolar CoCrFeMnNi composition and its selected subsystems, including CoCrFeNi alloy. What is more, it was also the very first study in which the possibility of employing the *reactive elements effect* (REE), known from conventional alloys, was considered as a mean of improving the oxidation resistance of the high-entropy alloys. In the case of the CoCrFeNi, the results indicated the formation of single-phase, chromia scales at temperatures of 650 and 750 °C, and showed the potential usefulness of the REE application in HEAs.

The subject of REE in high-entropy alloys has recently gained further attention from the researchers. Group of Lu et al. has recently published studies concerning the application of REE in Al–Co–Cr–Fe–Ni system. In the first of them, three alloys from $Al_x(CoCrFeNi)_{100-x}$ system with Al content of 15, 20 and 25 at.%, doped simultaneously with Y and Hf (both 0.02 at.%), were oxidized isothermally at 1100 °C for various time intervals between 1 and 1000 h [28]. In the case of the alloy with the highest Al content, a single-phase layer of Al_2O_3 was formed. Uniformly distributed grains rich in oxides of Hf and Y were observed on the surface and it was claimed that the oxide growth was controlled by inward diffusion of oxygen - a mechanism much more beneficial for the scales' adhesion than typically reported for HEA outward mechanism [16]. In the next study of the same team [29], the alloy with 15 at.% of Al was further investigated. The material was doped with 0.05 at.% of Y and Hf, followed by oxidation at 1200 °C, showing excellent oxidation kinetics and spallation resistance under isothermal conditions.

As can be seen from the literature review, while the current state of the art allows for a relatively thorough understanding of the substrate composition–oxidation product relation in HEAs, their oxidation behavior under thermal-cycling conditions which are much closer to the actual conditions observed in real-life applications has not been investigated at all. Considering the already apparent tendency for scale spallation observed even in isothermal studies, this can be considered a major limiting factor for the further development of high-entropy alloys. To address this issue, in the presented study the very first investigations of the oxidation behavior of the selected $Al_x(CoCrFeNi)_{100-x}$ ($x = 0$; 3; 6; 9; 12) under thermal-cycling conditions were undertaken. The choice of selected compositions allowed for covering the chromia-to-alumina former transition, as well as the transition from the FCC single-phase solid solution structure to multiphase alloys with Al-enriched B2-structured component. The obtained results clearly show a profound influence of the thermal-cycling conditions on the oxidation products, as well as limited resistance of the considered HEAs to scale spallation.

Experimental Procedures

The thermodynamic calculations enabling the determination of the expected equilibrium structures of the studied alloys were carried out with the use of Thermo-Calc software, coupled with the TCHEA4 database, dedicated strictly to the high-entropy alloys [30]. The materials were synthesized from the high-purity elements (> 99.8%, provided by Alfa Aesar) using the induction–melting technique. Each ingot was remelted three times to homogenize the alloy's composition and cast into the copper mold to form cylinders of 9 mm diameter. Melting and casting were conducted under a high-purity argon atmosphere. The ingots were then cut using electrical discharge machining into 1-mm-thick slices, followed by drilling with a 1 mm diameter carbide drill (provision for quartz suspension). Each sample was ground and polished using the standard Struers procedure, with the last polishing step being performed using 1 μm diamond paste. The microstructure of the alloys was examined with the use of scanning electron microscopy combined with the energy-dispersive X-ray spectroscopy (SEM, apparatus: JEOL JSM-6610LV scanning electron microscope equipped with EDS detector). The oxidation behavior under thermal cycling conditions was studied in laboratory air atmosphere, at the temperature of 1273 K, with the temperature being selected to ensure sufficiently high oxidation kinetics for both chromia- and alumina-forming compositions. All investigated samples were placed together in the common quartz boat, with each of them being hanged on a quartz suspension in the separate alumina crucible, which allowed collecting of the individual spalls. The thermal cycles were performed using subsequent cycles of 1 h heating and 20 min cooling at room temperature, with the furnace movement being controlled automatically. In total, 500 cycles were performed. Based upon the IR imaging, the minimum temperature obtained by the sample during cooling period was below 353 K. For each mass measurement, the samples together with crucibles were removed from the furnace. The mass measurements were taken using the laboratory weight of 0.00001 g sensitivity. The following values were collected:

- Net mass change (N):

$$N = \frac{m_{ni} - m_{n0}}{A} \tag{1}$$

- Spall mass change (S):

$$S = \frac{m_{si} - m_{s0}}{A} \tag{2}$$

- Gross mass change (G):

$$G = \frac{m_{gi} - m_{g0}}{A} \tag{3}$$

where m_{ni} is the mass of the sample after i-th cycle, m_{si} is the mass of the crucible after i-th cycle, m_{gi} is the mass of the sample and crucible after i-th cycle, m_{n0} is the

initial mass of the sample, m_{s0} is the initial mass of the crucible, m_{g0} is the initial mass of the sample and crucible and A is the total surface of the sample. Characterization of the substrate and obtained scales was performed using SEM/EDS methods and X-ray diffraction (XRD) (PANalytical X'Pert Pro PW 3710 X'Celerator) with standard Bragg–Brentano geometry. Analysis of the obtained results was conducted using X'Pert HighScore Plus 2.0 and Crystal Impact—Match!2 software. After analysis of the surfaces, the cross sections were prepared, with each sample being first subjected to nickel-plating, to increase the contrast between scale and the resin. To preserve the scales intact, the chemo-setting epoxy resin was used, to minimize the stresses during the embedding procedure. The metallographic preparation was performed using the same methodology as for the samples themselves. The cross sections were investigated with the use of SEM + EDS techniques, after being covered with the gold layer to limit samples' charging. For the selected $Al_6(CoCrFeNi)_{94}$ sample, additional examination with the use of transmission electron microscopy (TEM) was conducted. Observations of the cross sections of the selected $Al_6(CoCrFeNi)_{94}$ alloy after high-temperature oxidation test were performed using transmission electron microscopy combined with EDS analysis, with the use of TOPCON EM002B, JEOL JEM-4010HT microscope (operating at 400 keV, with the camera constant of 0.10694739 nm). The samples for TEM cross-sectional observations were prepared via the focused ion beam method (FB-2100, HITACHI) with a voltage of 40 keV and with the use of gallium ions.

Results and Discussion

Base Materials

The calculated isopleth of the Al–CoCrFeNi system together with the lines corresponding to the considered nominal composition is presented in Fig. 1.

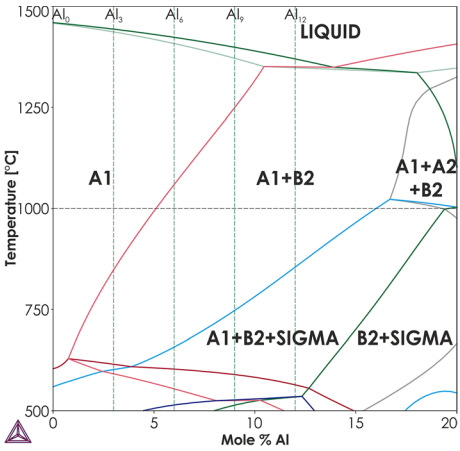

Fig. 1 Calculated isopleth of the Al–CoCrFeNi system

Table 1 Average compositions of the studied as-cast alloys, as-determined by the EDS area analysis

	Al	Co	Cr	Fe	Ni
CoCrFeNi	0.0	26.0	26.1	26.7	21.2
$Al_3(CoCrFeNi)_{97}$	3.1	24.5	24.5	23.9	24.3
$Al_6(CoCrFeNi)_{94}$	6.0	23.7	23.7	23.3	23.4
$Al_9(CoCrFeNi)_{91}$	9.2	23.1	23.1	22.6	22.3
$Al_{12}(CoCrFeNi)_{88}$	11.6	22.3	22.3	22.2	21.6

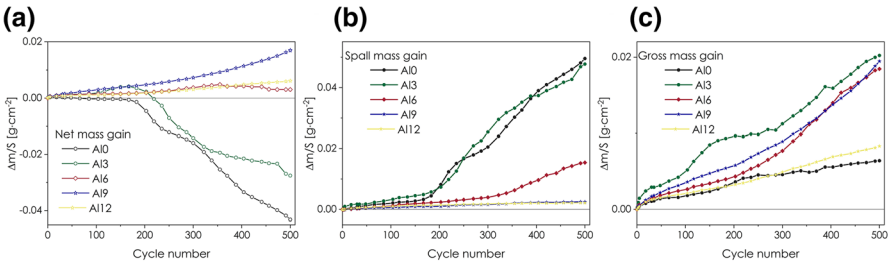

Fig. 2 Normalized mass changes: **a** net mass gain; **b** spall mass gain; **c** gross mass gain

As can be seen, with the increase in the Al content, within the assumed composition range a gradual transition from the single-phase FCC structure to the dual-phase, FCC + B2 structure is to be expected. At the experimental temperature of 1273 K, the Al solubility limit in the FCC solid solution is around 5 at.%, while at the solidus temperature, corresponding to the as-cast character of the materials, the solubility limit is slightly exceeding 10 at.%. Furthermore, based on the results of modeling, it can be expected that the forming ordered B2 phase will be significantly enriched with both Al and Ni. The average compositions determined from the EDS area analysis, are presented in Table 1.

As visible, the experimentally determined compositions are in a very good agreement with the nominal ones. Only in the case of the $Al_{12}(CoCrFeNi)_{88}$ the Al–Ni enriched, B2 precipitates were present, which is in line with the thermodynamic predictions for these materials at the solidus temperature.

Thermal-Cycling Measurement

Kinetic Measurements

The determined kinetics of the high-temperature oxidation under thermal-cycling conditions at 1273 K are presented in Fig. 2.

All three considered values: net (N), spall (S) and gross (G) mass change are presented. Based on the observed kinetics, the alloys can be divided into two groups: one consisting of CoCrFeNi (Al0) and $Al_3(CoCrFeNi)_{97}$ (Al3), and the second consisting of $Al_9(CoCrFeNi)_{91}$ (Al9) and $Al_{12}(CoCrFeNi)_{88}$ (Al12), with

$Al_6(CoCrFeNi)_{94}$ (Al6) exhibiting an intermediate behavior between both. In the case of Al0 and Al3, extensive spallation of the oxide scale is visible, which in both cases starts after *ca*. 180 cycles. The main difference between these two materials is the observed mass gain of Al3 on both N and G curves, on which the Al0 appears to spall the forming oxide scale from the very beginning. The Al9 and Al12, on the other hand, appear to exhibit almost identical and relatively good resistance to thermal shocks, with Al12 being superior to Al9 in terms of oxidation resistance. Still, both materials exhibit steady net mass gain over 500 cycles. The Al6 sample represents an intermediate case, with much lower spall values than Al0 and Al3, and significantly higher than both Al9 and Al12. It can be seen that after 350 cycles, its behavior changes, which is reflected in both a significant increase in spall value and gradually decreasing net mass change onwards. Consequently, it can be stated that Al0, Al3 and Al6 samples exhibit unsatisfactory long-term resistance to thermal shocks from the point of view of potential applications. An interesting comparison can be made with the Ni–Cr–Al-based alloys, which are commonly considered state-of-the-art conventional analogs of transition metal HEAs, including the oxidation behavior [20]. In most cases, these materials are designed as alumina formers, with typically higher Al content and operating temperature than materials presented herewith. Still, for the compositions characterized by similar Al and Cr content, e.g., the ones considered by Barrett et al. [31] (compositions '3' and '4', both containing 12 at.% of Al, and 13.2 and 18.4 at.% of Cr, respectively), at 1373 K the normalized spall mass gain after 500, 1-h long cycles was just ~ 2 times and ~ 7 times bigger, which considering the relatively big temperature difference of 100 K, may indicate a slight superiority of the Ni–Cr–Al alloys in terms of the spallation resistance. Another example can be the study by Fritscher et al. [32], who considered Ni–Cr–Al with and without Re + Ta refractory elements. In this study, the cyclic measurements were taken at 1273 K; however, each cycle consisted of 22 h of heating, followed by 2 h of cooling. Still, for the alloy with the closest Al content to the one considered herewith (14.4 at.% of Al), in all cases (with and without Re + Ta) the observed mass gains were almost an order of magnitude lower than the one presented for Al12. However, it should be remembered that both temperature and duration of the cycles strongly affect the kinetics of oxidation; therefore, further, comparative studies are necessary to draw conclusions regarding the relative oxidation resistance of alumina-forming HEAs and Ni–Cr–Al alloys.

Analysis of the Oxidation Products - Surface

The XRD diffractograms, together with the identified phases, are presented in Fig. 3.

In all cases, complex, multiphase oxide scales are formed. For Al0, Al3 and Al6 alloys, mainly the spinel phases are observed, with only a small content of Cr_2O_3 being visible in Al0 diffractogram. However, for Al9 and Al12, the additional presence of chromia becomes much more visible, with a characteristic peak ca. 24.5° becoming apparent. Furthermore, for Al9 and Al12, the Al_2O_3 becomes distinguishable, suggesting the transition of the system to the alumina-forming region. These features can be easily correlated with the drastically improved oxidation behavior of the Al9 and Al12 samples. It should be noted that in the case of rocksalt-structured

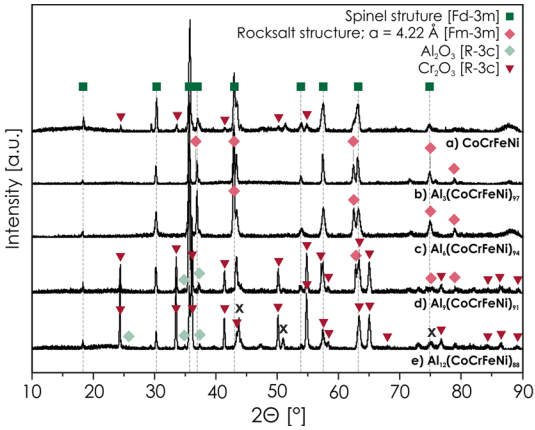

Fig. 3 XRD diffractograms of the studied alloys after 500, 1-h thermal cycles at 1273 K

and spinel-structured phase, only the general symmetry is given, with the reason being evident after the analysis of the SEM + EDS data of the surfaces of the oxidized samples (Fig. 4).

As can be seen, especially in the case of Al0, Al3 and Al9 samples, the EDS point analysis indicates the presence of multicomponent, often near-equimolar phases, which approach the definition of the high-entropy oxides. In fact, in some cases (e.g., Al0) the composition is remarkably similar to that of the known high-entropy spinels, such as $(Co,Cr,Fe,Mn,Ni)_3O_4$ [33, 34]. Such behavior drastically differs from the one reported for the similar compositions under isothermal conditions. For instance, for the $Al_8(CoCrFeNi)_{92}$, $Al_{10}(CoCrFeNi)_{90}$ and $Al_{12}(CoCrFeNi)_{88}$ alloys studied by Butler et al. [21] at 1323 K, after 50 h primarily phase-pure scales of chromia, chromia, and alumina, respectively, were reported, with only a trace content of spinel phase being present in $Al_8(CoCrFeNi)_{92}$ sample. Similarly, Holcomb et al. [27] reported chromia scale formation on the CoCrFeNi alloy after oxidation at 750 °C for 1100 h. It can be postulated that the observed formation of multicomponent, complex phases is a characteristic feature of the HEAs under thermal-cycling conditions, where the highly non-equilibrium conditions, combined with a constant quenching from the high temperatures, favor the formation of such phases, as the contribution of the configurational entropy to the total Gibbs free energy of oxide phases becomes much more prominent at high temperatures, similarly as in

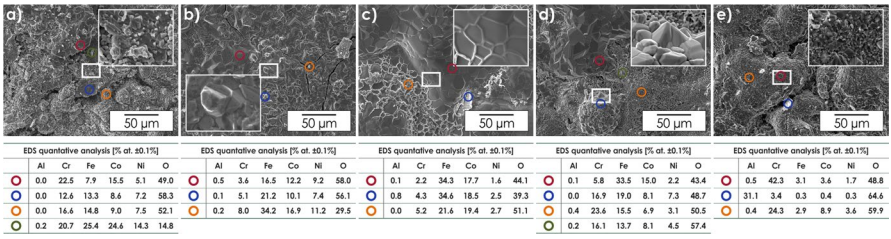

Fig. 4 Results of the SEM + EDS analysis of the studied alloys after 500, 1-h thermal cycles at 1273 K: **a** CoCrFeNi; **b** $Al_3(CoCrFeNi)_{97}$ (Al3); **c** $Al_6(CoCrFeNi)_{94}$; **d** $Al_9(CoCrFeNi)_{91}$; **e** $Al_{12}(CoCrFeNi)_{88}$

high-entropy alloys, and the quenching process allows preserving of such structures between the cycles [35]. The observed complexity of the oxide scales, especially when contrasted with the results reported for the isothermal conditions [21], further supports the notion that the studied HEAs exhibit insufficient resistance to thermal shocks, as such conditions clearly inhibit the formation of otherwise observed continuous, protective chromia and alumina scales. It remains to be seen whether such behavior will extend on the Al–Co–Cr–Fe–Ni compositions with higher content and therefore activity of the Al.

Analysis of the Oxidation Products - Cross Section

The SEM micrographs of the polished cross sections are presented in Fig. 5, with the insets representing the structures near the middle of the samples, together with the corresponding EDS results. As visible, the structure of the substrates significantly changes during the oxidation. The most striking feature is probably the presence of huge internal nitridation zones in all Al-containing samples, which in the case of the Al3, Al6 and Al9 occurs across the whole cross section. As indicated by the results of the EDS analysis presented in the insets, both chromium and aluminum (AlN) nitrides are formed, although in the case of chromium the EDS indicates the oxygen presence in the precipitates. It is worth noting that the stoichiometry of this oxynitrade appears to be atypical, as the ratio of Cr:N:O is reproducible across all samples and is *ca*. 16:6:1. For the Al0 sample, the extent of chromium nitridation appears to be significantly smaller than in the case of Al-containing compositions, which may suggest that the presence of Al escalates the process. Also, the limited uptake of nitrogen for this material, when compared with other samples, can be used to explain its relatively low gross mass change. Curiously, in the case of Al12 sample, the highest Al content the internal nitridation zone is relatively the smallest, as the formation of Al- and Ni-enriched B2 phase in the middle of the substrate appears to completely suppress the formation of nitrides. Therefore, it can be stated that the aluminum nitride competes for the Al with the B2 phase. It is further supported by the fact that despite the equilibrium solubility limit of Al in FCC phase being around 5 at.% at 1273 K (Fig. 1b), no signs of B2 precipitates can be found in the Al6 and Al9 samples, as the formation of AlN depletes the metallic matrix with Al.

In order to visualize the complexity of the formed scales, higher-magnification micrographs of the oxide layers, together with the results of EDS point analysis, are presented in Fig. 6. For the Al0 sample, the EDS analysis confirms the presence of Cr_2O_3. It can be also seen that the spinel phase visible in the diffractogram contains mostly Cr with the content of Ni being the smallest. On the other hand, Ni appears to be the main component of the rocksalt-structured phase.

In both Al3 and Al6 samples, the complexity of the scale is much higher, with the scale having a layered structure with visible rehealing effects. The internal layer closest to the oxide/substrate interface consists exclusively of Cr_2O_3, which can be easily seen on the EDS map (Fig. 7a). The outer layer consists of two main phases - the rocksalt-structured one, consisting mainly of Ni and Co, similarly as in Al0, and the spinel phase, which in this case has a close-to-equimolar ratio of all elements in this system, making it effectively a high-entropy oxide. In Al9, the

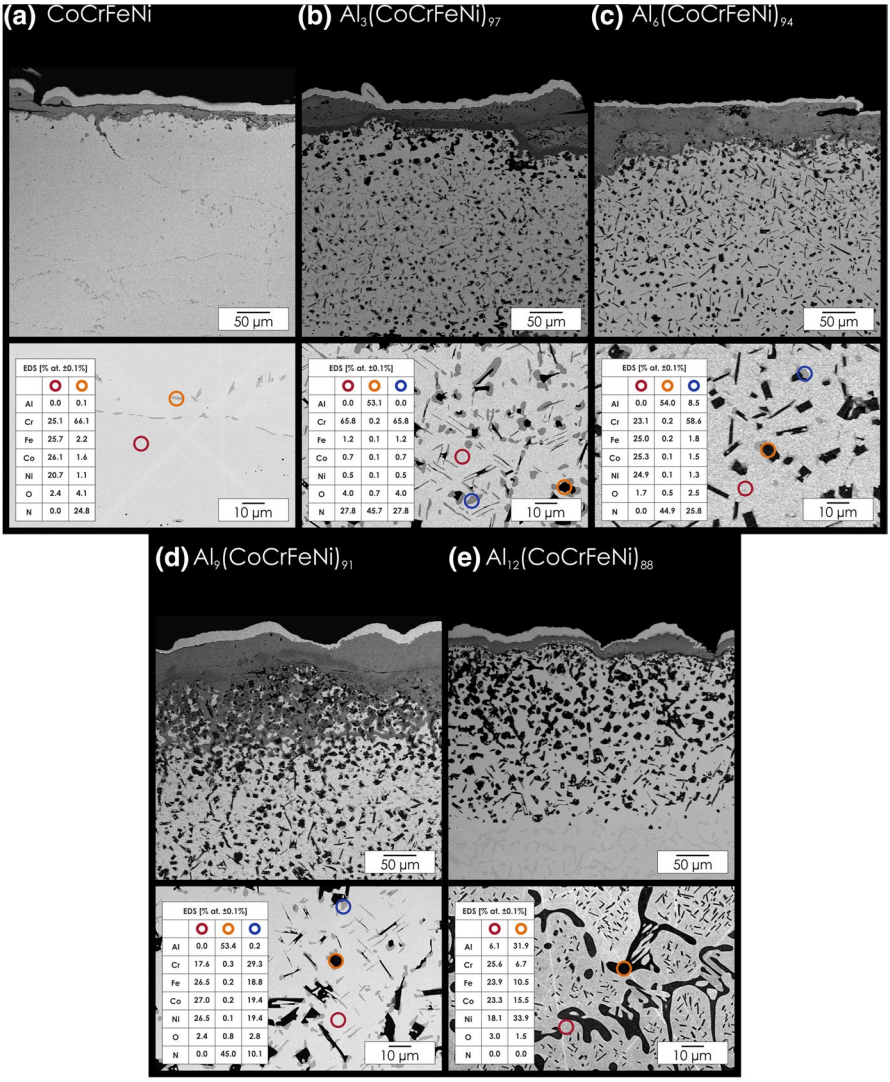

Fig. 5 SEM micrographs of cross sections of the oxidized $Al_x(CoCrFeNi)_{100-x}$ ($x=0$; 3; 6; 9; 12) samples after 500, 1-h cycles at 1273 K. The insets present the microstructures of the metallic substrates, together with the corresponding results of EDS analysis

composition of the scale changes notably. The spinel phase is based mainly on the Fe and Co, and the Cr_2O_3 does not form a layer on the oxide/substrate interface as is the case in Al3 and Al6. On the opposite, the EDS mapping (Fig. 7b) indicates the formation of chromia in the outer part of the scale which is of importance. Additionally, in Al9 sample, the Al finally appears to take part in the scale formation, with a thin, almost continuous Al-rich layer being visible close to the scale/substrate interface, signaling the transition to the alumina-forming region of the

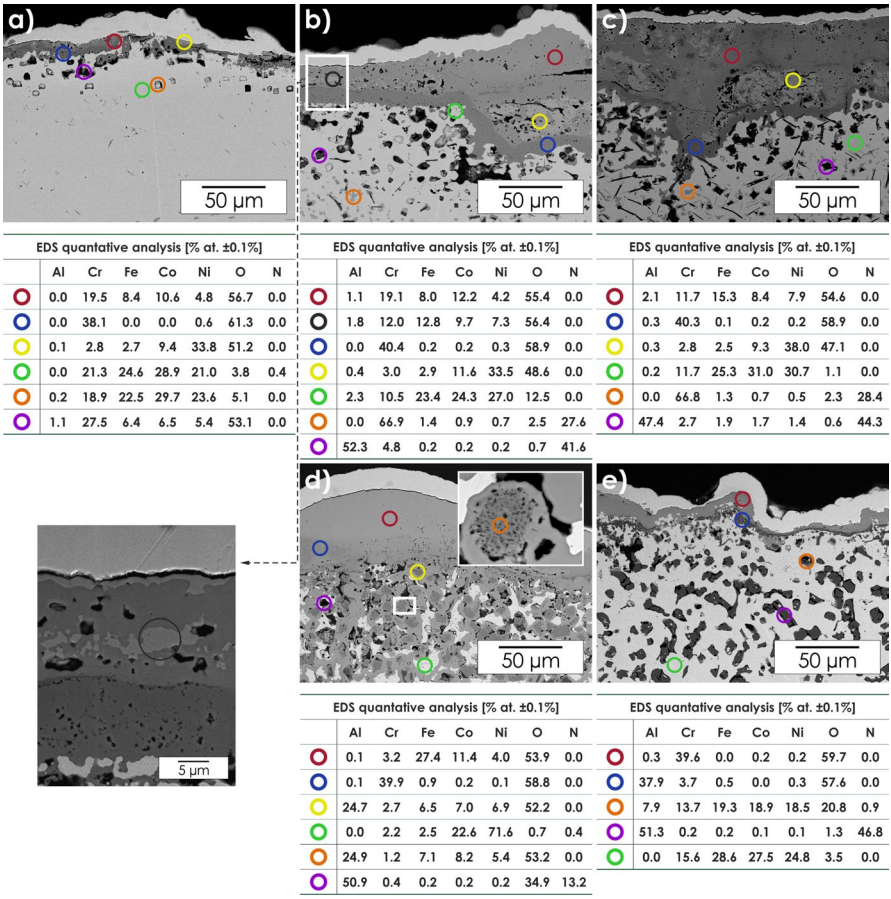

EDS quantative analysis [% at. ±0.1%]

	Al	Cr	Fe	Co	Ni	O	N
	0.0	19.5	8.4	10.6	4.8	56.7	0.0
	0.0	38.1	0.0	0.0	0.6	61.3	0.0
	0.1	2.8	2.7	9.4	33.8	51.2	0.0
	0.0	21.3	24.6	28.9	21.0	3.8	0.4
	0.2	18.9	22.5	29.7	23.6	5.1	0.0
	1.1	27.5	6.4	6.5	5.4	53.1	0.0

EDS quantative analysis [% at. ±0.1%]

	Al	Cr	Fe	Co	Ni	O	N
	1.1	19.1	8.0	12.2	4.2	55.4	0.0
	1.8	12.0	12.8	9.7	7.3	56.4	0.0
	0.0	40.4	0.2	0.2	0.3	58.9	0.0
	0.4	3.0	2.9	11.6	33.5	48.6	0.0
	2.3	10.5	23.4	24.3	27.0	12.5	0.0
	0.0	66.9	1.4	0.9	0.7	2.5	27.6
	52.3	4.8	0.2	0.2	0.2	0.7	41.6

EDS quantative analysis [% at. ±0.1%]

	Al	Cr	Fe	Co	Ni	O	N
	2.1	11.7	15.3	8.4	7.9	54.6	0.0
	0.3	40.3	0.1	0.2	0.2	58.9	0.0
	0.3	2.8	2.5	9.3	38.0	47.1	0.0
	0.2	11.7	25.3	31.0	30.7	1.1	0.0
	0.0	66.8	1.3	0.7	0.5	2.3	28.4
	47.4	2.7	1.9	1.7	1.4	0.6	44.3

EDS quantative analysis [% at. ±0.1%]

	Al	Cr	Fe	Co	Ni	O	N
	0.1	3.2	27.4	11.4	4.0	53.9	0.0
	0.1	39.9	0.9	0.2	0.1	58.8	0.0
	24.7	2.7	6.5	7.0	6.9	52.2	0.0
	0.0	2.2	2.5	22.6	71.6	0.7	0.4
	24.9	1.2	7.1	8.2	5.4	53.2	0.0
	50.9	0.4	0.2	0.2	0.2	34.9	13.2

EDS quantative analysis [% at. ±0.1%]

	Al	Cr	Fe	Co	Ni	O	N
	0.3	39.6	0.0	0.2	0.2	59.7	0.0
	37.9	3.7	0.5	0.0	0.3	57.6	0.0
	7.9	13.7	19.3	18.9	18.5	20.8	0.9
	51.3	0.2	0.2	0.1	0.1	1.3	46.8
	0.0	15.6	28.6	27.5	24.8	3.5	0.0

Fig. 6 SEM micrographs of cross sections of the oxidized $Al_x(CoCrFeNi)_{100-x}$ ($x=0$; 3; 6; 9; 12) samples after 500, 1-h cycles at 1273 K. **a** CoCrFeNi; **b** $Al_3(CoCrFeNi)_{97}$; **c** $Al_6(CoCrFeNi)_{94}$; **d** $Al_9(CoCrFeNi)_{91}$; **e** $Al_{12}(CoCrFeNi)_{88}$. The corresponding results of the EDS point analysis are also provided

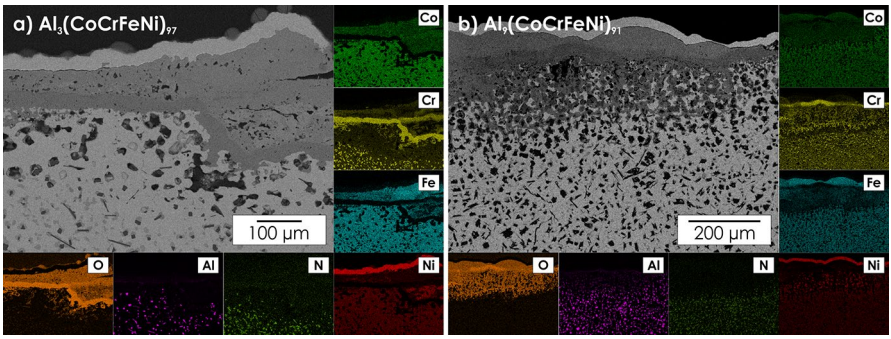

Fig. 7 Results of EDS mappings of the oxidized: **a** $Al_3(CoCrFeNi)_{97}$; **b** $Al_9(CoCrFeNi)_{91}$

phase diagram. This correlates nicely with the marked improvement in the oxidation kinetics (Fig. 2.) and is also in good agreement with the isothermal results by other authors [21] and predictions of the Giggins–Pettit theory [25]. A significant internal oxidation zone, together with the already mentioned, even bigger internal nitridation zone, is also visible directly beneath the scale. The matrix residues visible between the oxide precipitates consist mostly of Ni and Co, suggesting that the oxides of these two elements are characterized by the lowest stability in the system. Finally, for the Al12 sample, much different behavior is visible. The scale is much thinner and the observed oxide phases, as indicated by EDS, are mainly Cr_2O_3 and Al_2O_3. Such scale's composition explains the distinguishably favorable oxidation behavior of the $Al_{12}(CoCrFeNi)_{88}$ in comparison with other considered materials.

TEM Analysis

The $Al_6(CoCrFeNi)_{94}$, representing the intermediate case between the behavior of Al0/Al3 and Al9/Al12, was selected for further investigations with the use of TEM technique. The TEM image of the prepared sample, together with the corresponding EDS points, is presented in Fig. 8. As can be seen, the TEM results indeed support the presence of multicomponent oxide phases, close to the definition of high-entropy oxides. The formation of such phases is therefore the major difference in comparison with the isothermal behavior of these alloys [21]. What is also visible is the tendency toward the formation of the Co- and Ni-rich phases closer to the oxide/substrate interface, which agrees with the observations made for the Al9 sample, where Co- and Ni-enriched matrix remnants were observed in the internal oxidation zone.

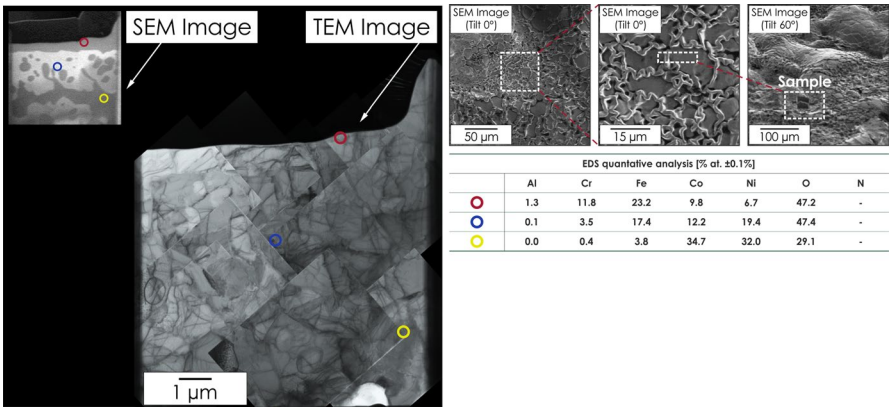

Fig. 8 TEM micrography with the corresponding EDS point analysis of the oxidized $Al_6(CoCrFeNi)_{94}$ sample

Conclusions

The oxidation behavior of $Al_x(CoCrFeNi)_{100-x}$ ($x = 0; 3; 6; 9; 12$) high-entropy alloys was studied at the temperature of 1273 K, for the first time under thermal-cycling conditions in the air atmosphere. The choice of the compositions supported by the thermodynamic modeling, allowed covering the transition region between FCC and B2 + FCC structures, as well as a transition region between alloys nominally classified in the literature as chromia and alumina formers. The measured kinetics indicate a drastic change in the oxidation behavior and thermal shock resistance between CoCrFeNi and $Al_3(CoCrFeNi)_{97}$, and $Al_9(CoCrFeNi)_{91}$ and $Al_{12}(CoCrFeNi)_{88}$ compositions, with $Al_6(CoCrFeNi)_{94}$ exhibiting an intermediate behavior between both extremes. The observed extensive scale spallation, especially in the low Al content compositions, indicates a limited usefulness of the studied materials for the real-life, high-temperature structural applications. The analysis of the oxidation products shows an unusually complex structures of the scales formed under thermal-cycling conditions, which is in contrary to majority of reported isothermal data, where pure phase chromia and alumina scales are reported. A profound amount of the investigated scales consist of various, multicomponent spinel phases, which in some cases conform to the definition of the high-entropy oxides, exhibit close-to-equimolar, 4-or-more-component compositions. In all samples, the presence of Cr_2O_3 was observed, with additional Al_2O_3 contribution in $Al_9(CoCrFeNi)_{91}$ and $Al_{12}(CoCrFeNi)$, correlating with their improved corrosion behavior. What is worth noting, in all samples extensive internal nitridation zones can be observed, which in $Al_3(CoCrFeNi)_{97}$, $Al_6(CoCrFeNi)_{94}$ and $Al_9(CoCrFeNi)_{91}$ spreads across the whole substrate. The Al appears to be the driving force for the nitridation process; however, in the case of $Al_{12}(CoCrFeNi)_{88}$, the formation of the Al-rich B2 phase inside the bulk completely suppresses the nitridation process. The obtained results, the very first concerning the oxidation behavior of HEAs under thermal-cycling conditions, show that the oxidation mechanisms and products in HEAs are extremely dependent on the oxidation conditions, and the behavior reported in isothermal studies does not translate to non-equilibrium cyclic ones. Considering the prospects of applying HEAs as high-temperature structural materials, it seems that a much bigger emphasize should be put in future on non-isothermal examinations, as reported behavior may become a limiting factor in envisioned applications.

Acknowledgements This research was supported by the Polish National Science Center (NCN) under project No. PRO-2015/17/N/ST8/00094.

References

1. K.H. Huang and J.W. Yeh, *Hsinchu: National Tsing Hua University*. (1996).
2. J. W. Yeh, S. K. Chen, et al., *Advanced Engineering Materials.* **6**, (5), 299–303 (2004).
3. B. Cantor, I. T. H. Chang, et al., *Materials Science and Engineering: A*. **375–377**, 213–218 (2004).
4. J. W. Yeh, S. K. Chen, et al., *Metallurgical and Materials Transactions A*. **35A**, 2533–2536 (2004).
5. J. W. Yeh, *Annales de Chimie-Science des Materiaux.* **31**, 633–648 (2006).
6. J. Chen, X. Zhou, et al., *Journal of Alloys and Compounds.* **760**, 15–30 (2018).
7. D. B. Miracle and O. N. Senkov, *Acta Materialia.* **112**, 448–511 (2016).
8. B. Cao, T. Yang, et al., *MRS Bulletin.* **44**, 854–859 (2019).
9. Y. Zhang, T. T. Zuo, et al., *Progress in Materials Science.* **61**, 1–93 (2014).
10. A. C. Yeh, T. K. Tsao, et al., *International Journal of Metallurgical & Materials Engineering.* **1**(107), 1–4 (2015).
11. H. M. Daoud, A. Manzoni, et al., *JOM.* **67**, 2271–2277 (2015).
12. Y. Lu, Y. Dong, et al., *Scientific Reports.* **4**, 6200 (2014).
13. A. M. Manzoni, S. Singh, et al., *Entropy.* **18**, 104 (2016).
14. C. C. Tung, J. W. Yeh, et al., *Materials Letters.* **61**, 1–5 (2007).
15. S. Singh, N. Wanderka, et al., *Acta Materialia.* **59**, 182–190 (2011).
16. J. Dąbrowa, G. Cieślak, et al., *Intermetallics.* **84**, 52–61 (2017).
17. M. C. Gao and J. Qiao, *Metals.* **8**, 108 (2018).
18. Y. F. Kao, T. J. Chen, et al., *Journal of Alloys and Compounds.* **488**, 57–64 (2009).
19. Y. F. Kao, S. K. Chen, et al., *Journal of Alloys and Compounds.* **509**, 1607–1614 (2011).
20. T. M. Butler, J. P. Alfano, et al., *JOM.* **16**, 246–259 (2014).
21. T. M. Butler and M. L. Weaver, *Journal of Alloys and Compounds.* **674**, 229–244 (2016).
22. W. Kai, F. P. Cheng, et al., *Journal of Alloys and Compounds.* **836**, 155518 (2020).
23. J. Zhu, S. Lu, et al., *Oxidation of Metals.* **94**, 265–281 (2020).
24. S. Abbaszadeh, A. Pakseresht, et al., *Surfaces and Interfaces.* **21**, 100724 (2020).
25. C. S. Giggins and F. S. Pettit, *Journal of the Electrochemical Society.* **118**, 1782–1790 (1971).
26. T. M. Butler and M. L. Weaver, *Metals.* **6**, 222 (2016).
27. G. R. Holcomb, J. Tylczak, and C. Carney, *JOM.* **67**, 2326–2339 (2015).
28. J. Lu, Y. Chen, et al., *Corrosion science.* **170**, 108691 (2020).
29. J. Lu, Y. Chen, et al., *Corrosion science.* **174**, 108803 (2020).
30. Thermo-Calc Software TCHEA: High Entropy Alloys database version 4.1, June 2020
31. C. A. Barrett and C. E. Lowell, *Oxidation of Metals.* **11**(4), 199–223 (1977).
32. K. Fritscher, O. Schubert, et al., *Oxidation of Metals.* **78**(1), 63–82 (2012).
33. J. Dąbrowa, M. Stygar, et al., *Materials Letters.* **216**, 32–36 (2018).
34. M. Stygar, J. Dąbrowa, et al., *Journal of the European Ceramic Society.* **40**, 1644–1650 (2020).
35. C.M. Rost, Entropy-Stabilized Oxides: Explorations of a Novel Class of Multicomponent Materials, North Carolina State University, 2016.